AIAA 2011-3735

Force Measurement Techniques and Preliminary Results Using Aerogels and Ferroelectrics for Dielectric Barrier Discharge Actuators

Ryan Durscher* and Subrata Roy†
Computational Plasma Dynamics and Test Facility, Applied Physics Research Group
Mechanical and Aerospace Engineering Department
University of Florida, Gainesville, FL 32611-6300

This paper presents experiments carried out on dielectric barrier discharge plasma actuators. Two areas concerning these actuators are addressed in this work: First, two different experimental techniques used to measure the induced body force are compared. A high precision force balance is used to make a direct measurement of the thrust produced which is then compared with a control volume analysis on data obtained through particle image velocimetry. For the direct measurements the effect of varying the actuator plate length upon which the induced flow acts is also investigated. The results from these tests show that the length of the actuator plate is most influential at higher voltages with the measured force increasing as much as 20% as the length of the plate is decreased. When the two methods are compared against each other, good agreement is found given that the control volume size has a sufficient downstream extent. In the second part of the paper, materials with extreme relative dielectric constants (ε) are investigated for performance. Specifically, the use of silica aerogels (ε ~ 1.1) and ferroelectric dielectrics (ε = 1750) are examined. The silica aerogel was found to have a strong effect on thrust generation as compared to the other dielectrics tested. However, the power supplied to the ferroelectric actuator manifests itself primarily as heat generation with no noticeable thrust measured. Especially due to its minimal actuator weight penalty and higher thrust, actuators made with silica aerogel may be quite useful for practical applications.

Nomenclature

f	=	measured thrust, g
F_x	=	tangential component of force normalized by actuator length, mN m^{-1}
F_y	=	normal component of force normalized by actuator length, mN m^{-1}
H	=	height of control volume above the dielectric surface, mm
I	=	instantaneous applied input current, A
l	=	length of electrode, cm
L	=	length of dielectric plate, cm
P	=	total power delivered to the actuator, W
P_{inf}	=	ambient pressure, Pa
t	=	thickness of dielectric substrate, mm
U	=	induced flow velocity, m s^{-1}
V	=	instantaneous applied input voltage, V
w	=	width of electrode, cm
W	=	width of control volume, mm
x_0	=	starting x-location for control volume integrals, mm
y_0	=	starting y-location for control volume integrals, mm
ΔP	=	differential pressure, Pa
ε	=	relative dielectric constant
ρ	=	fluid density, kg m^{-3}

* Graduate Student, Student Member AIAA, dursch@ufl.edu
† Associate Professor, Associate Fellow AIAA, roy@ufl.edu

$\rho_{dielectric}$= density of dielectric, g cm^{-3}

I. Introduction

In its simplest form the single dielectric barrier discharge (SDBD) plasma actuator consists of two conducting electrodes placed asymmetrically on either sides of a dielectric material. Upon the application of a sufficiently high AC voltage (and resulting electric field ~30kV/cm at atmospheric pressure) across the electrodes a weakly ionized plasma forms on the surface of the dielectric. The plasma imparts an electro-hydrodynamic (EHD) body force on the neutrally charged ambient air through a collisional energy transfer mechanism which is yet to be understood.

The aerodynamic benefits of the induced body force from these actuators were first publicized in the mid 1990s. Roth et al.[1,2] was among the first to utilize the DBD actuator to manipulate the boundary layer on a flat plate over a range of freestream velocities. Since then these actuators have been used for control devices on stationary[3-5] and oscillating airfoils[6], landing gear noise reduction[7], low pressure turbine blades[8,9], and bluff bodies[10]. As continued progress is made in the DBD actuator design, there is no doubt that new applications will continue to emerge.

Much of the progress that has been made stems from parametric studies which have focused on aspects such as applied voltage/frequency, dielectric material, electrode arrangement and geometry in an effort to achieve an optimized device.[11-20] Typically, in order to evaluate the relative impact of these parameters either the induced body force is measured directly using a high resolution (mg) force balance, or the resulting velocity is extracted using techniques such as pitot probes, particle image velocimetry (PIV), and laser Doppler velocimetry (LDV). In some cases the measured velocity has been used to calculate the body force based on a control volume analysis on the flow field.

This paper is broken into two parts. The first part focuses on a comparative study of the aforementioned experimental techniques used to measure the induced body force. Inferred forces determined from a control volume analysis on the flow field obtained through PIV are compared to direct force measurements. The influence of the plate size on the direct force measurement is also investigated. The second part explores materials with extreme relative dielectric constants (ε). Specifically, the performance of silica aerogels and ferroelectric dielectrics in the DBD design are investigated. The nominal dielectric constants for these two materials are at the very extrema of dielectrics thus far investigated in the reported literature with their respective constants being ~1.1 and 1750. The low density of the silica aerogel and its operational impact on the actuator's weight is also demonstrated and discussed.

II. Experimental Arrangement

A. Plasma Actuator Design and Discharge Generation

The following actuator setup describes the actuator configurations used in the comparison of force measurement techniques. Due to the relatively small size of the material used to test the dielectric extremes, the dimension and power schemes were slightly modified. Differences will be noted where present.

A cross sectional schematic of the DBD plasma actuator used in these experiments is shown in figure 1a. The actuator consists of two thin (70 μm) copper electrodes placed asymmetrically on either side of the dielectric material with no horizontal gap between the two electrodes. The dielectric in this case was a 3 mm thick (*t*) sheet of acrylic which has a nominal relative dielectric constant, ε, of 3. The width, *w*, of the upper electrode was 0.5 cm while the lower electrode's width is 2 cm. Both electrodes have a length, *l*, of 12 cm. Standard electrical tape in combination with epoxy covered the encapsulated electrode to avert an unwanted discharge on the lower surface. Similarly an 84 μm thick piece of Kapton was placed on the opposite side of the exposed electrode covering any discharge that may occur. The actuator depicted in figure 1b shows the dimensions of the dielectric used in the

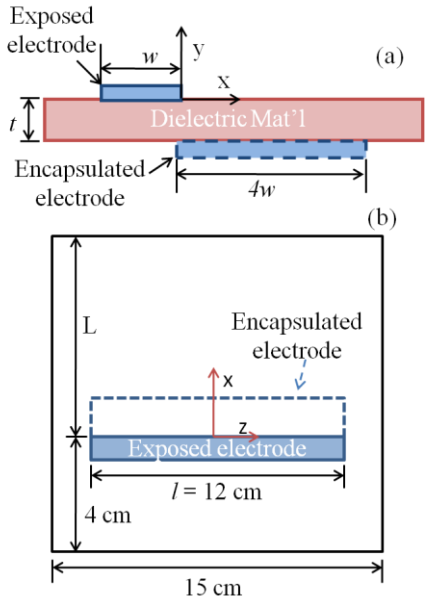

Figure 1. Schematic of DBD plasma actuator: a) side view and b) top view

actuator plate length tests, where the effect on the thrust was investigated by shortening the actuator's plate length, *L*. The dimensions of the actuator plate used in the PIV measurements will be discussed later.

In order to ionize the surrounding air, the exposed and grounded electrodes were each supplied with high voltage signals that were 180° out of phase. The sinusoidal signals originated from an arbitrary waveform generator (Tektronix AFG3022B). The input signals were further amplified by a dual output audio amplifier (QSC RMX 2450) which was then stepped up using Corona Magnetics, Inc. high-voltage, high-frequency power transformers (figure 2). Two frequencies, 7 kHz and 14 kHz, were investigated.

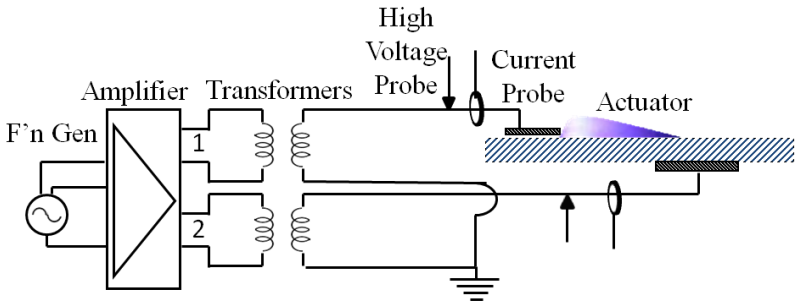

Figure 2. Circuit schematic used to generate a dual powered DBD plasma discharge

The voltage and current supplied to the actuators were monitored using high voltage (Tektronix P6015A) and current probes (Pearson Electronic 2100). In order to calculate the delivered power, the voltage and current waveforms were captured using a digitizing oscilloscope (Tektronix DPO3014). In a single acquisition the oscilloscopes captured 1 million points for each waveform at a sampling rate of 250 MSa/s. For each input voltage 10 acquisitions where recorded. This corresponds to 280 and 560 periods over which the calculated power is averaged for 7 kHz and 14 kHz waveforms, respectively. The total power, *P*, delivered to the plasma actuator was considered to be a superposition of the power supplied to each electrode. The average real power was numerically calculated by multiplying the instantaneous voltage, V_i, by the instantaneous current, I_i, and then summing and dividing by the total number of samples, *N*. The indices 1 and 2 in equation 1 correspond to the respective circuit branches in figure 2.

$$P = \frac{1}{N}\left(\sum_{i=1}^{N} V_{1,i} I_{1,i} + \sum_{i=1}^{N} V_{2,i} I_{2,i}\right) \tag{1}$$

B. Direct Force Measurements

Direct force measurements were obtained using an Ohaus precision balance (Adventurer™ Pro AV313C). The actuators were mounted to the scale by an acrylic stand which protruded though a small opening in a Faraday's cage. The cage was used to shield the balance from any electromagnetic noise present due to the high electric fields required to generate the plasma discharge. To prevent ambient room currents from influencing the sensitive scale (resolution is 1 mg), the entire setup was housed in a large quiescent chamber with dimensions 0.61 x 0.61 x 1.22 m (width x depth x height). The chamber was slightly vented, but not enough that noticeable amounts of ozone (an unavoidable consequence of the plasma formation) spilled out into the laboratory air. Ozone levels in the room are continuously monitored using an Aeroqual SM-70 ozone monitor. Thin insulated wire (34 AWG) was used to connect the high-voltage input leads to the actuator in order to limit the rigidity of the wire from influencing the reading. For each input voltage, 15 measurements were recorded from the

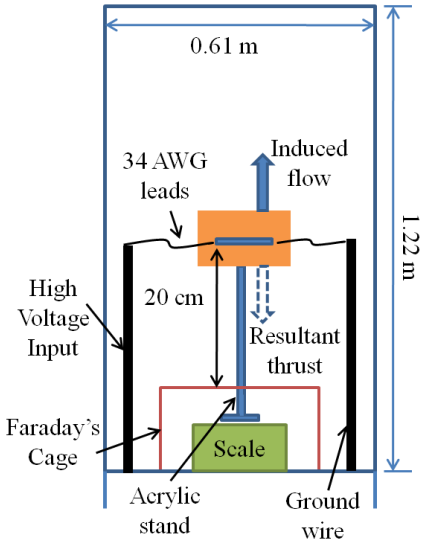

Figure 3. Experimental setup schematic for direct force measurement.

scale over a 30 second span once an initial stable reading was reached. The uncertainty associated with a given force measurement is 4% (to 95% confidence).

C. Control Volume Analysis

1. Flow Field Measurements

Two-component particle image velocimetry (PIV) was used to generate time-averaged, spatially resolved data of the induced flow due to the plasma actuator. These averaged vector fields were then used for the control volume analysis. The plasma actuator geometry is similar to that described above in the plasma actuator design section; however the dielectric plate upon which the actuator was built was much larger. The dimensions of the plate are 30 cm x 30 cm with the electrodes placed in the center. The actuator was set-up in the same quiescent chamber as described above.

A Nd:YAG, dual cavity pulsed 532 nm laser (New Wave Research Solo PIV II 30) was used to generate a light sheet along the centerline of the actuator normal to the span. This illuminated the vaporized Ondina oil used to seed the chamber. The oil was vaporized using a TSI atomizer (Model 9302) which, when pressurized at 25 psi, produces a droplet with a mean diameter of ~0.8 μm.[21] Ondina is assumed to be dipole neutral and thus least affected by the high electric field near the actuators. *LaVision*'s adjustable light sheet optics allowed for fine adjustments to the waist of the laser sheet, which had an estimated thickness of 1 mm. For each run, 300 image pairs were taken at a repetition rate of 7.2 Hz. The time separation (*dt*) between laser pulses was adjusted accordingly depending on the induced flow velocity. In general, the *dt* was set to maintain a maximum particle displacement of 5 to 7 pixels. *LaVision*'s ImagerPro X 4M (2048 x 2048 pixels) camera fitted with a 105 mm lens was used to capture the PIV images. The field of view for each image was approximately 48 mm x 48 mm (x, y).

LaVision's DaVis 7.2 PIV software package was used to calibrate, capture, pre-process, process and post-process the PIV images. Image calibration was performed with a 40 mm x 40 mm, two-tiered calibration plate. The following outlines the steps implemented in determining the vector field from the raw camera images. The first step in the processing of the PIV images was to calculate an average image intensity for each frame in a given data set. These averages were then subtracted from the raw images in order to increase the relative contrast between the particles and the background. A local particle intensity correction is then applied in which the particle intensities are normalized over a window of 4 pixels. This allowed for smaller particles to contribute more effectively in the correlation.[22] Having masked the surface of the actuator, each image pair was then subjected to a cross-correlation multi-grid process. The correlation process consisted of an initial pass with a 32 x 32 pixel interrogation window with a 50% overlap, followed by two refining passes with 16 x 16 pixel widows again with 50% overlaps. For the initial pass a 1:1 Gaussian weight was applied to the integration widows, while a 2:1 was applied on the refining passes. This resulted in a vector field resolution of 0.19 mm. Outliers were detected and removed using a median filter in between multi-grid passes as well as on the final vector field.[22]

2. Inferred Force Calculation

The rectangular control volume as depicted in figure 4 was applied to the time-averaged velocity field generated from the PIV measurements. The analysis is similar to that of Hoskinson et al.[17] and Baughn et al.[23], however, their control volumes were drawn to create a distinction between the plasma body force and the wall shear force. In this analysis we are only interested in the reaction forces, F_x and F_y, imparted to the dielectric, therefore the control volume used here does not include the aforesaid distinction. Starting with the conservation of momentum and simplifying by assuming time independence, constant pressure, and no flow beneath the actuator, one arrives at an analytical expression for the reaction forces. The x and y components of the force normalized by the actuator length are given in equation 2a and 2b, respectively.

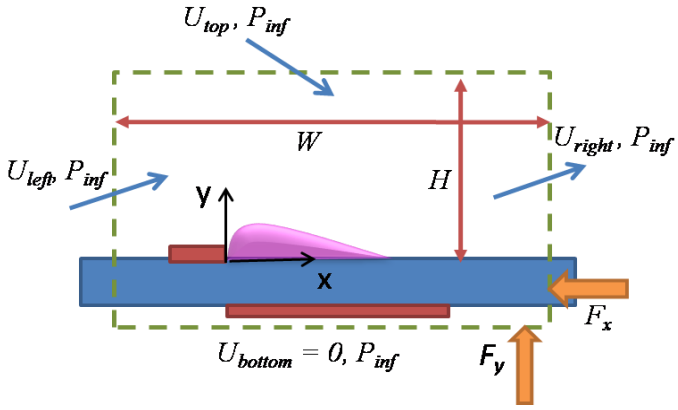

Figure 4. Schematic of control volume used to calculate reaction forces induced by the plasma discharge.

$$F_x = -\int_{y_0}^{H} \rho U_{x,left}^2 dy + \int_{x_0}^{W} \rho U_{x,top} U_{y,top} dx + \int_{y_0}^{H} \rho U_{x,right}^2 dy \qquad (2a)$$

$$F_y = -\int_{y_0}^{H} \rho U_{y,left} U_{x,left} dy + \int_{x_0}^{W} \rho U_{y,top}^2 dx + \int_{y_0}^{H} \rho U_{y,right} U_{x,right} dy \qquad (2b)$$

III. Results

The following section is broken into two parts. The first segment, subsection A, presents a comparison study on induced thrust measurements made between a direct force measurement and that inferred through a control volume analysis. Subsection B describes performance characterization using dielectric materials with extreme relative dielectric constants (1750 and ~1.1) in the DBD design.

A. Force Comparison

1. Actuator Plate Length

In order to evaluate the effect of the actuator's plate length (*L*), as shown in figure 1b, different plate lengths were tested. The same actuator was used throughout the experiments with the plate length *L* being reduced each time. Lengths corresponding to 15, 10, 5, and 2.5 cm were investigated over a range of voltages. A plate length of 15 cm was chosen as to mimic the plate length of the actuator used in the control volume analysis. A limiting length of 2.5 cm was imposed to avoid the possibility of arcing around the dielectric substrate, since the encapsulated electrode itself is 2 cm wide. 10 and 5 cm were chosen arbitrarily as incremental lengths.

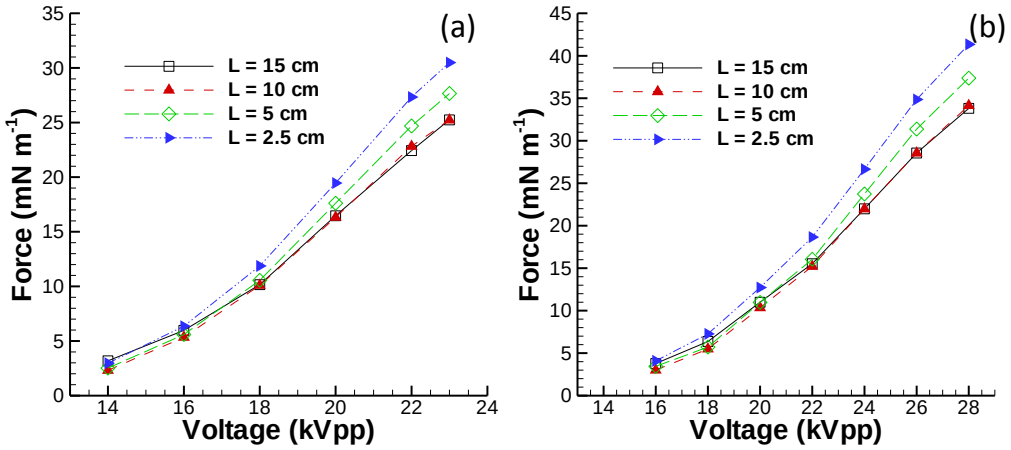

Figure 5. Force measurements over a range of input voltages with varying actuator plate lengths: a) 14 kHz and b) 7 kHz

The results of this study, presented in figure 5, indicate that there is little variation in the resultant force regardless of the length of the plate for lower input voltages. This trend does not hold, however, as the voltage increases. At the higher voltages investigated, an increase in thrust is observed as the actuator's plate length is decreased. This increase is independent of the two frequencies investigated. At the maximum voltages tested a difference of 5 and 7 mN/m was measured between plate lengths of 15 and 2.5 cm for 14 and 7 kHz, respectively. This corresponds to a 20% increase in measured thrust in both cases. Such a relatively large discrepancy could prove problematic when trying to compare between different researchers' results.

Since the longer plate lengths (*L* = 15 and 10 cm) converge to a single value, it is believed that these lengths provide a more accurate representation of the true net thrust (= plasma force – viscous drag) produced. The velocity profile for the larger plates will have a significantly longer length to develop over allowing saturation of the resulting viscous drag, and also providing a more comparable flow field with that of the PIV experiments. A plot of power versus applied voltage confirms these notions (figure 6). One would expect that the force would remain constant for a given supplied power. As shown in figure 6, the actuator consumes the same amount of power regardless of the length of the plate indicating that the power delivered to the plasma load remains the constant. By

reducing the plate size one is only causing changes in the viscous drag component for the same actuator setup. Contrarily, one way to extract the majority of the plasma force without the viscous drag would be to use a minimum plate length resulting in minimum drag loss.

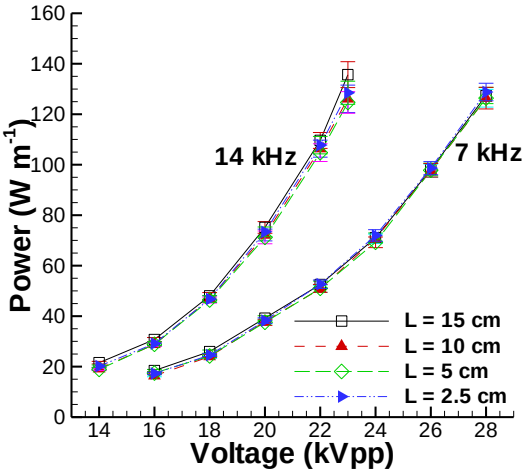

Figure 6. Power dissipation as a function of voltage for different plate lengths.

As stated previously the chamber in which the scale is housed is only slightly vented to prevent obnoxious amounts of ozone from continuously spreading into the laboratory. As a consequence one could argue that for particularly long runs of the actuator that the air chemistry inside of the chamber is being modified. To test this argument, two tests were carried out over a range on input voltages. In one case the 0.74 m^2 door to the chamber was closed during testing, while it was left wide open in the other. The measured thrust from these tests are shown in figure 7, where "not vented" and "vented" correspond to the door being closed and open, respectively. As one can see, the resultant thrust was nearly identical regardless of ventilation. This result would likely change if the volume of the quiescent of chamber was reduced, though the results seem indifferent for the current experimental setup.

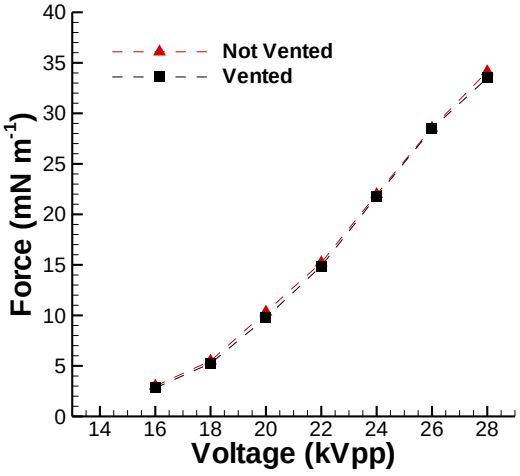

Figure 7. Effect of a vented versus unvented chamber on the induced thrust. The plate length was 10 cm and the input frequency was 7 kHz.

2. Control Volume Extracted Forces

In order to extract the reaction forces on the control volume, the integrals on the right-hand side of equations 2a and 2b were numerically integrated in Matlab using the time averaged PIV data. Both composite trapezoidal rule (a 2nd order accurate method) and composite Simpson's rule (3rd order accurate) integration schemes were applied. While both methods yielded nearly identical outcomes, the following results were obtained using the trapezoidal rule. It was found that the starting x-location, x_0, in the integrals had little influence on the resultant force calculated as long as it was chosen behind the edge of the exposed electrode (i.e. $x_0 < x = 0$, referring to figure 4). The starting y-location, y_0, was chosen arbitrarily below the dielectric material such that $y_0 < 0$ (figure 4). The starting locations used were - 5.0 mm and -0.1 mm corresponding to x_0 and y_0, respectively. Also, it is pertinent to note that a constant fluid density (ρ) is assumed. This assumption was also made by Hoskinson et al.[17] based on prior experimental data from Enloe et al.[24]. In this prior work it was estimated that the density fluctuations near the actuator were less than 2% of ambient. Here fluid density was taken as 1.184 kg m^{-3} which corresponds to a laboratory temperature of 25 ^oC.

Figure 8 depicts a plot of the tangential force component, F_x, and how it varies with the width (W) and the height (H) of the control volume (referring to figure 4). The applied voltage was 15, 19, and 22 kVpp at an input frequency of 14 kHz. Although not shown, the normal force component (F_y) exhibits similar characteristics as do the force components for a lower driving frequency, 7 kHz. The plot indicates that the force is independent of the height above the dielectric surface in which the control volume is taken beyond a given point (10 mm for these cases). This point corresponds to the total encapsulation of the induced wall jet's "boundary layer". The boundary layer created by the jet increases with both applied voltage and downstream location. However, for the range of voltages investigated the boundary layer was less than 10 mm thick for the given field of view. More important than the height of the control volume is its width, as figure 8 reveals. The calculated thrust is highly dependent on the point at which the control volume ends. If the width is too small the thrust may be grossly over predicted as compared to a much wider control volume.

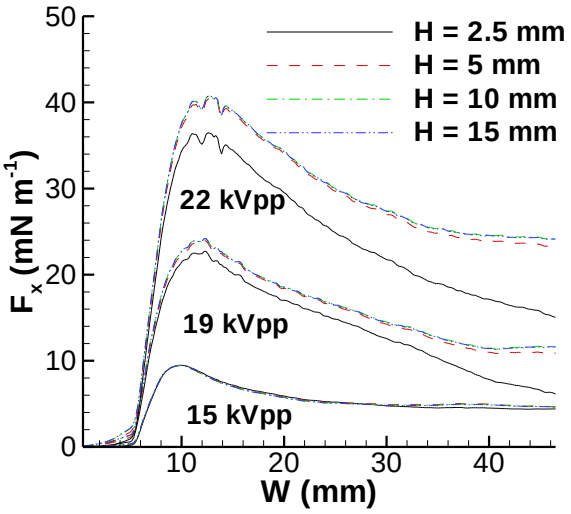

Figure 8. Resultant tangential force component for a 15, 19, and 22 kV_{pp} input voltage at 14 kHz as function of the width (W) for varying heights (H) of the control volume.

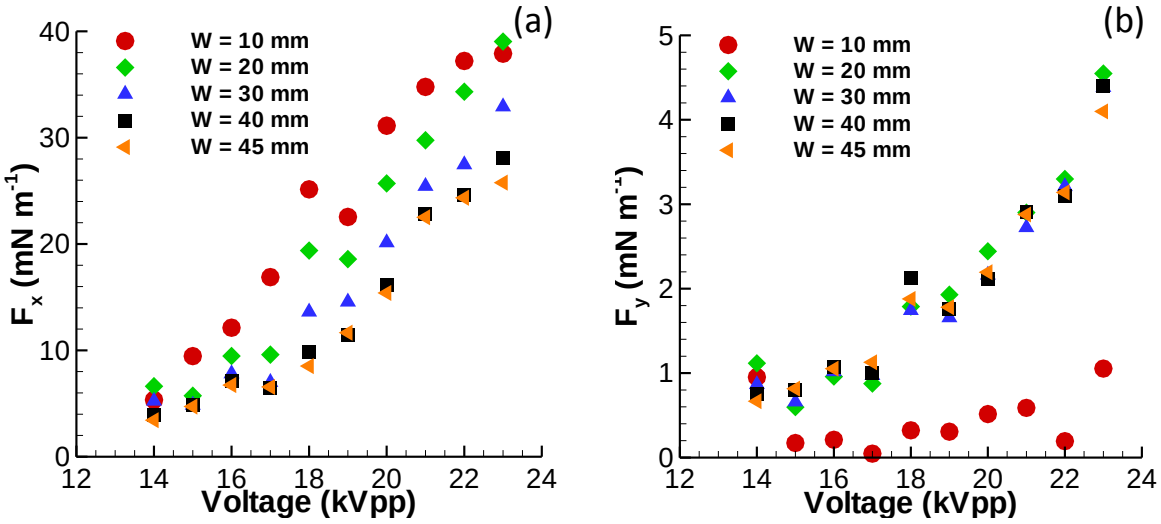

Figure 9. Forces calculated from a control volume analysis as a function of voltage for various widths of the control volume: a) tangential component of force (F_x) and b) normal component of force (F_y).

The tangential and normal force components are plotted in figures 9a and 9b, respectively, over the range of input voltages investigated. At each voltage, the force was extracted for five different control volume widths from data similar to figure 10. The vertical dashed lines in figure 10 correspond to control volume widths of 10, 20, 30, 40, and 45 mm. The height of the control volume chosen was 10 mm, which for reasons previously discussed is a suitable choice. Over the range of supplied voltages the same trend holds, in that the resultant tangential force has a strong dependency on the width of the control volume. This dependence becomes more pronounced at higher voltages. The calculated forces do begin to converge, however, as the downstream extent of the control is increased. Based on the current results a downstream extent of ~35 mm is necessary to provide consistent results. This

convergence/asymptotic behavior can also be seen in figure 8. A similar trend was observed for a driving frequency of 7 kHz.

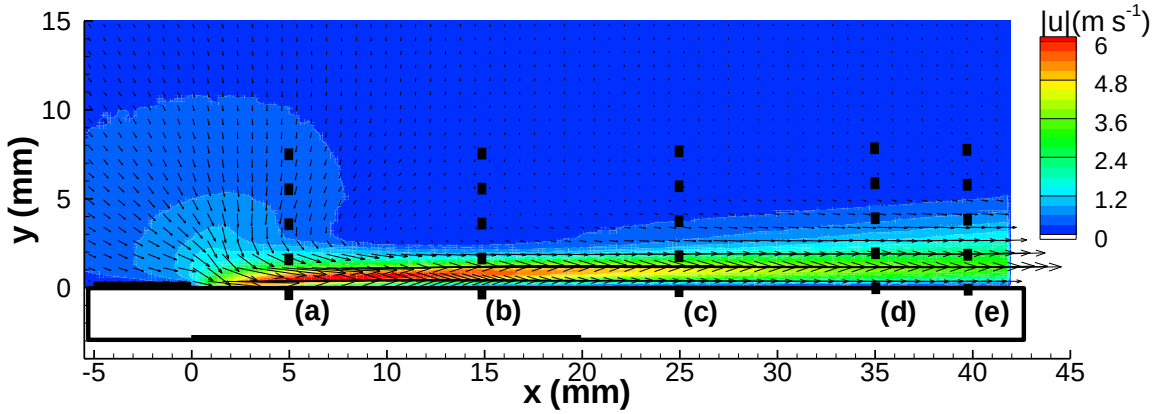

Figure 10. Velocity magnitude contour for 21 kV_{pp} input driven at 14 kHz. The dashed lines labeled (a) through (e) correspond to control volumes widths ($W = x-x_o$) of 10, 20, 30, 40, and 45 mm, respectively.

The normal force component deviates from this trend with its values remaining approximately constant as the width of the control volume is increased (figure 9b). The exception, however, to this observation is the smallest control volume plotted (W = 10 mm). Regardless, the magnitude of the normal component is significantly less than that of the tangential. With such a large disparity between the normal and tangential components, it is assumed that the normal component will have a negligible impact on the direct force measurement and there should be a reasonably good agreement between the two techniques.

To validate the results of the PIV data, velocity measurements were made 15 mm downstream of the exposed electrode using a pitot probe (figure 11). The pitot probe was constructed out of a modified glass Pasteur pipet with an inner and outer diameter of 1.2 and 1.5 mm, respectively. The pressure measurements were made using a Furness Controls FCO332 differential manometer calibrated to ±25 Pa with a ±10 V output. Each data point represents the average of 120 voltage reading recorded at a sampling rate of 15 Hz using a National Instruments data acquisition module (PCI-6133). The differential pressure, ΔP, measurements were converted to velocities using equation 3 where density was again taken as 1.184 kg m^{-3}. Reasonably good agreement is seen between the two data sets. The slight difference between the two profiles height and magnitude could be attributed to the relatively large area of integration of the inner diameter of the pitot probe used. Further experiments will be carried out using a smaller probe.

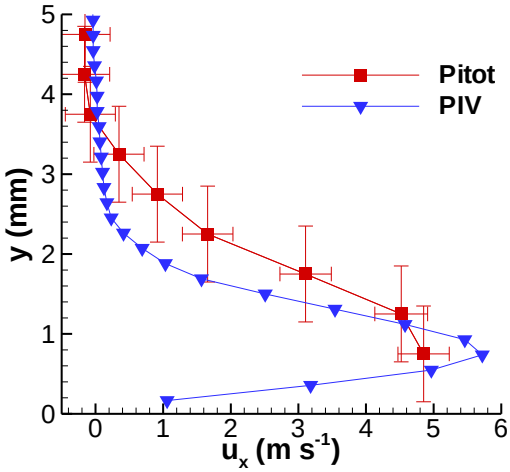

Figure 11. Comparison between pitot measurements and PIV profiles taken 15 mm downstream of exposed electrode for an applied voltage of 21 kVpp at 14 kHz. The vertical error bars on the pitot measurements indicate the inner diameter of the probe used.

$$U_X = \sqrt{2\Delta P / \rho} \qquad (3)$$

3. Comparison of measurement methods

A comparison between the control volume analysis and the direct force measurement is shown in figure 12. Two different control volume widths (W = 40 and 20 mm) are presented, as well as the direct force measurements with an actuator plate length of 10 cm (note that the difference between L = 10 and 15 mm was negligible). Results indicate that the measured and inferred forces are in good agreement over the entire voltage range for the wider (40 mm) control volume. Result also show that if the control volume is of insufficient size, that force may be over predicted and eludes that there is a minimum length downstream of the actuator that the control volume needs to consider. That length however is directly tied to the applied voltage as there is a decent agreement for the smaller control volume width at lower input voltages. Based on these results a downstream extension of ~35 mm is recommended. Again these trends are consistent for a 7 kHz input frequency as well.

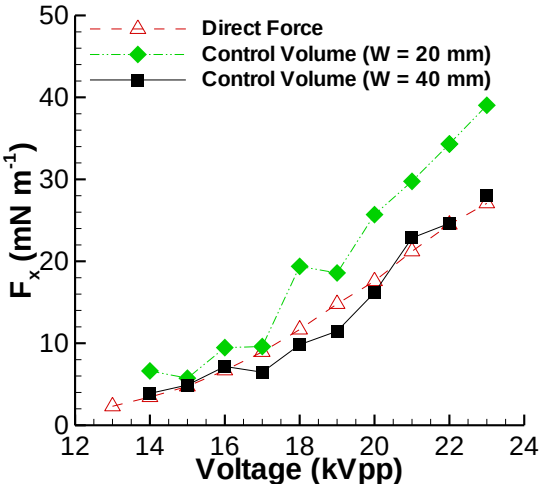

Figure 12. Comparison between direct force measurements and those inferred from a control volume analysis. The driving frequency was 14 kHz

B. Extreme Materials

1. - Ferroelectric

In a prior experimental investigation Thomas et al.[19] showed that for a fixed plate thickness and frequency, the saturation thrust (or maximum force achieved) decreased as the dielectric constant increased from 2 to 6. To thoroughly test this trend we investigated the use of a ferroelectric (Modified Lead Zirconate-Titanate, PZT) material as a dielectric. The ferroelectric sample had a nominal relative dielectric constant of 1750. The dimensions of the ferroelectric sample were 40 mm x 12 mm (x, y), which is significantly smaller than that of the acrylic plates described above. As such the electrode geometry was slightly modified to that described in figure 1. The exposed and encapsulated electrodes were each 5 mm wide and the thickness of the material was 3 mm. Also a high voltage amplifier (Trek 30/20C) replaced the transformers and audio amplifier shown in figure 2 with the encapsulated electrode now being grounded.

The ferroelectric material allowed for a discharge ignition at a much lower input voltage has compared to materials of the similar thickness with lower dielectric constants. A representative picture of the discharge generated is shown in figure 13a for an input voltage of 3.5 kVpp. As shown in the figure the discharge is concentrated around the exposed electrode's edge and never propagates downstream as would a device constructed from a lower dielectric constant. Attempts were made to apply higher voltages to the actuator, however dielectric heating became a problem with temperatures reaching ~200 ^{o}C after only 10's of seconds of operation. At this point, keeping the adhesively backed copper tape adhered to the surface was difficult. Since the thrust produced is directly tied to voltage, over the range of inputs allowable (1.5 to 4.0 kVpp at 5 kHz) no force was measured.

With no force being achieved, the dielectric heating of the device was investigated. A FLIR A320 infrared camera was used. The camera has a spectral range of 7.5-13 μm and a pixel resolution of 320 x 240 pixels. The ambient humidity (55% RH), distance from actuator (0.33 m), and material emissivity were all considered in determining the surface temperature. The emissivity of ferroelectric material was found to be 0.96 ± 0.02 and was

determined by heating the dielectric to a uniform temperature and comparing the cameras readout with a surface mounted thermocouple. As mentioned in the previous paragraph, the high temperatures observed during initial tests were found to exceed the boundaries set by the current actuator configuration, as such the operational voltage/frequency regimes were set as to not exceed these limits. Temperature measurements were made over a range of voltages (1.5 to 4.0 kVpp) at 5.0 kHz as well as over a range of frequencies (DC to 14 kHz) at 3.5 kVpp. Figure 13b shows a representative surface temperature distribution after 300 seconds of operation. Looking at a time trace (figure 14a) for a point taken at x = 12.5 mm and y = 1.5 mm we see that the surface temperature as a sharp initial increase and then gradually rises to its steady state temperature. The profiles presented in figure 14a are consistent with that of Joussot et al.[25] and Jukes et al.[26]. The measurements shown in figure 14a correspond to an initial 5 seconds of non-actuation after which the device was turned on for 300 seconds. Once turned off, another 40 seconds of data acquisition continued. Noting the seemingly strong dependence on frequency, a plot of the temperature rise after 300 seconds (at x = 12.5 mm, y = 1.5 mm) as a function of power shows a linear relationship proportional to 0.87 ^{o}C W^{-1}m (figure 14b). This proportionality is independent of the input frequency and voltage, a trend also observed by Joussot et al.[25] However, as shown in figure 14a for a constant voltage one may reach the same surface temperature faster using a higher frequency. The results indicate a possibility of operating at an even higher frequency (~MHz) to generate thermal loading at a faster timescale (ms).

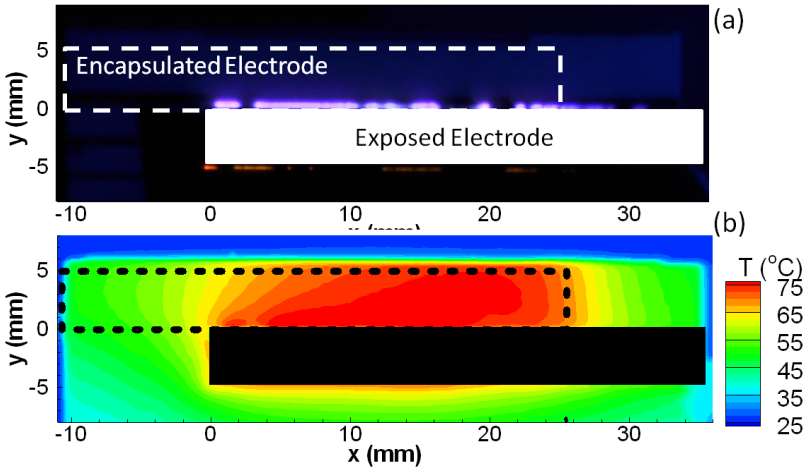

Figure 13. Visual picture of plasma discharge (a) and corresponding surface temperature (b) for a 3.5 kVpp, 5kHz sinusoidal input. Temperature measurement was take after 300 seconds of operation

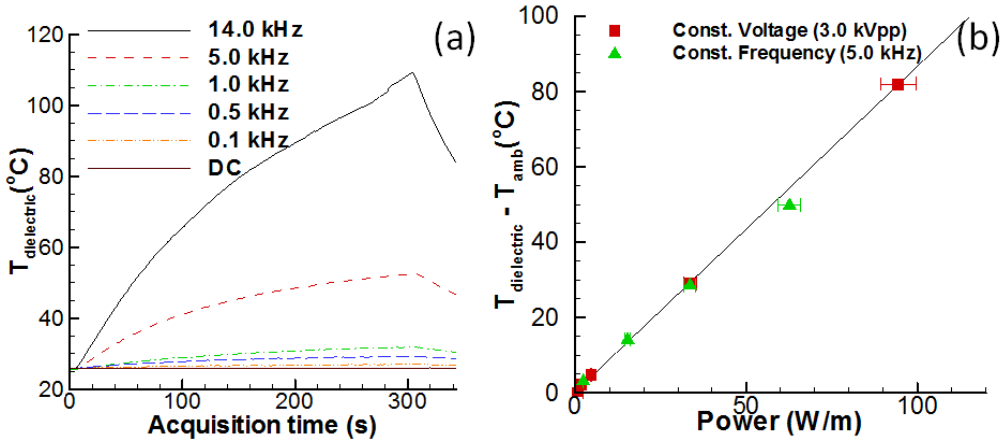

Figure 14. a) Surface temperature as a function time about point 12.5, 1.5 mm (x,y) for varying frequencies and b) temperature rise in the dielectric after 300 seconds of actuation for a modulated frequency at 3 kVpp (red square) and a modulated voltage at 5kHz (green diamond).

2. Silica Aerogel

Silica aerogel was used to investigate the low end of the dielectric spectrum. The properties of this unusual material are quite amazing and numerous open sources may be found online that describe these properties as well as how silica aerogels are manufactured. Here we provide a basic description and only focus on the properties relative to these experiments. In general silica aerogels consist of a complex microstructure of silicon dioxide in which air occupies a majority of it volume. For the samples tested, ~95% of the dielectric's volume was air resulting a density ranging from 0.04 to 0.12 g cm^{-3} with results being reported for samples having a density of 0.11 g cm^{-3}. Silica aerogels in this range of densities have a relative dielectric constant of 1.1-1.2.[27] Shown in figure 15 is an image of a plasma discharge on an initial sample of aerogel as well as an image of the sample from which results are reported. The initial samples tested were relatively small which prohibited the use of the same electrode arrangement as in the force comparison section. Larger samples were obtained (figure 15b, t = 6 mm, 8 cm diameter) and the electrode layout shown in figure 1a was used for the reported data. The length of the electrode, *l*, was reduced to 4.0 cm.

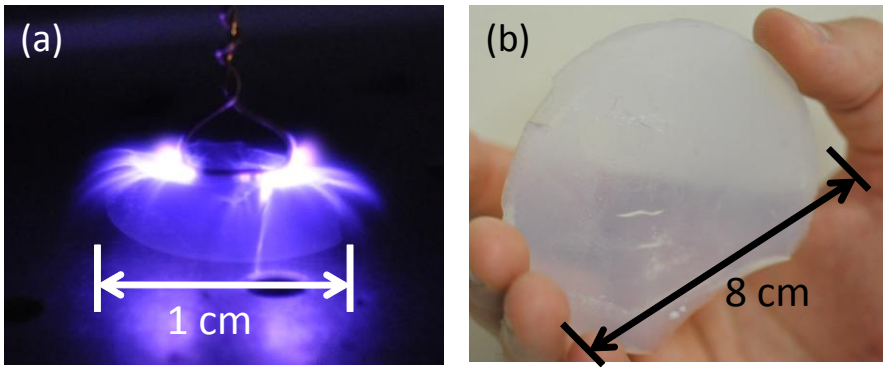

Figure 15. Plasma discharge (a) on a preliminary sample of silica aerogel used as a proof of concept and (b) a larger sample of aerogel used in reported data.

As previously mentioned in a prior optimization study Thomas et al.[19] showed that higher voltages can be applied resulting in larger forces when using a material with a lower dielectric constant. With that in mind a material with a dielectric constant approaching 1 would certainly be advantageous. This is demonstrated in figure 16 in which the induced forces produced by actuators using acrylic and aerogel dielectrics are compared. The thickness of each sample was 6 mm. The thrust produced by the acrylic actuator was measured directly, where the silica aerogel case is extracted from PIV measurements using the control volume analysis described above. As with before the force was found to converge for a control volume width around 40 mm. The driving frequency for these cases was 14 kHz. Interestingly for this frequency, the induced force for an acrylic actuator asymptote at about 34 mN m^{-1} while the silica aerogel demonstrates a much higher thrust. It should be noted that the voltage range in this report was limited to 36 kVpp though higher voltages should have been possible. It is also notable that for a given voltage the acrylic actuator generates more thrust up to its saturation point.

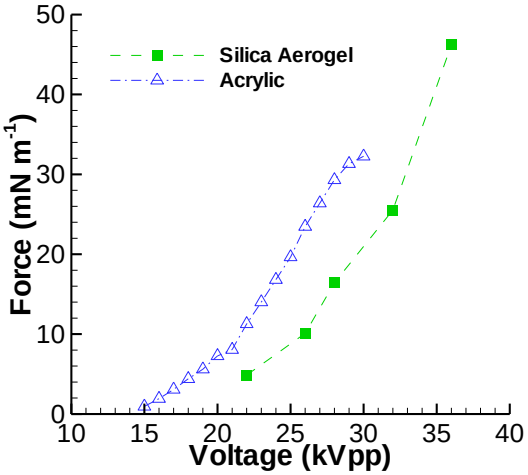

Figure 16. Comparison between resultant force measurements for actuators constructed out of silica aerogel and acrylic (t = 6 mm, 14 kHz).

An added benefit of the aerogel is its low density, a parameter that would be critical when applying these actuators to medium to small/micro air vehicles. The benefits of using a thicker dielectric in the DBD actuator design were also shown by Thomas et al.[19] in their optimization study. Force data for varying dielectric thicknesses is shown in figure 17a for an actuator constructed out of a single sheet of acrylic, as well as a single data set for a 170 μm thick Kapton (ε = 3.5)

dielectric. A constant driving frequency of 14 kHz was used. Consistent with previously reported results[19], figure 17a shows that by increasing the thickness of the dielectric layer larger voltages can be applied to the actuator. The additional voltage increases the maximum thrust achieved

A tradeoff of increasing the dielectrics thickness, however, is that the weight of the actuator also increases. Although this would be of little consequence for large scale applications, it could prove detrimental at smaller scales needing to benefit from the increased body force associated with thicker dielectrics. Figure 17b re-plots the data shown in figure 17a on a thrust to actuator weight ratio defined by equation 4. The thrust to weight ratio in equation 4 divides the force generated by the density of dielectric times its volumetric footprint. All dimensions are in centimeters (referring to figure 1) and the density of acrylic and Kapton were taken as 1.20 and 1.42 g cm^{-3}.

$$Force/Weight = \frac{f}{t \times l \times (w+4w) \times \rho_{dielectric}} \qquad (4)$$

For the conventional dielectrics tested (Kapton and acrylic) a thinner dielectric is clearly beneficial based on a force to weight basis. However, when the silica aerogel is consider the benefits of this extremely low density material are clearly shown (figure 17b). For a constant material thickness (t = 6 mm), the thrust to weigh ratio measured has increased from 9×10^{-3} (at 30 kVpp) to 1.4×10^{-1} (at 36 kVpp) for the acrylic and aerogel samples, respectively. The force to weight ratio for Kapton is 7×10^{-2} at 12 kVpp.

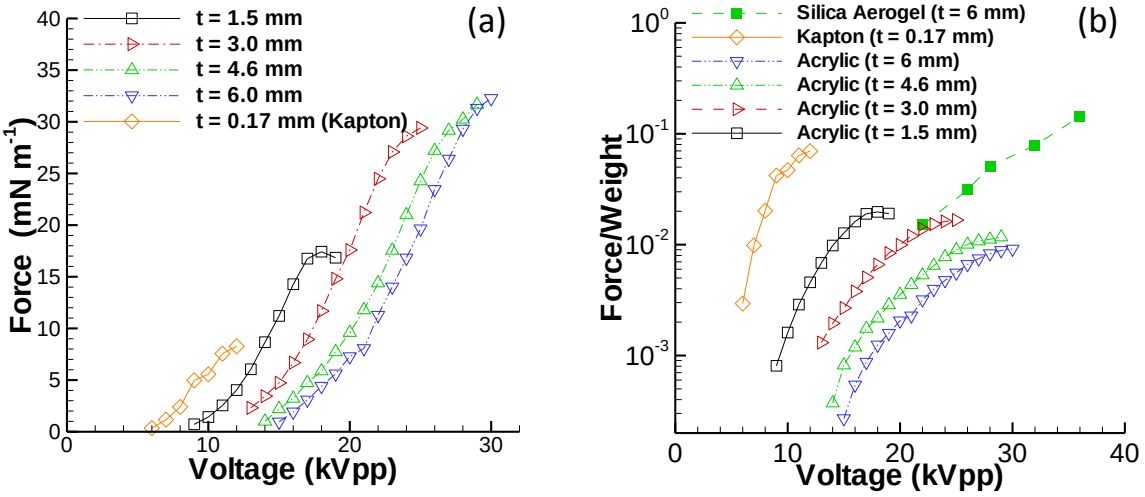

Figure 17. Effect of the dielectric thickness as a function of voltage (a) on thrust production for acrylic and Kapton actuators, and (b) the ratio of force generated to the actuator weight for various dielectrics.

IV. Conclusion

The effect of varying the plate length upon which the plasma induced wall jet acted was investigated using a direct force balance. At the upper range of the voltages investigated, an increase in force was observed as the plate length was decreased. The force was nearly identical for 10 and 15 cm lengths, but an increase in thrust of 20% was observed as the plate length was reduced to 2.5 cm. Based on these findings, one needs to take the plate's length into consideration when making comparisons between various researchers' reported data. Particle image velocimetry measurements were also made on an actuator with the same dimensions. These measurements provided time averaged data sets of the induced flow field. The velocity fields were then subjected to a control volume analysis to infer the resultant forces acting on the rectangular volume. The results of the analysis indicated a strong dependency on the size of the considered volume with a particular emphasis on the width of it. For a far enough downstream extension (~35 mm) the inferred force was found to converge. When compared with the direct thrust measurements, the calculated tangential force agreed well regardless of input voltage if the control volume extended far enough downstream.

Dielectrics possessing relative dielectric constants of ~1.1(silica aerogel) and 1750 (ferroelectric) have also been investigated. For the latter case no force was observed over the range of tested voltages and frequencies. Significant heating of the dielectric was observed using infrared thermometry. The results indicate the possibility of operating at a higher frequency (~MHz) to generate thermal loading at a faster timescale (~ms). The silica aerogel, however, was found to a have a strong effect on the thrust generation. Significantly higher voltages were sustainable for such a low dielectric constant compared to other materials of similar thickness. The aerogel's minimal weight penalty and higher thrusts may lend itself to many practical applications such as medium to small/micro air vehicles.

Acknowledgements

This work was sponsored in part under Air Force Office of Scientific Research Grants #FA9550-09-1-0372 and #FA9550-09-1-0615 monitored by Dr. Doug Smith and Charles Suchomel.

References

[1]Roth, J.R, , Sherman, D., and Wilkinson, S. "Boundary layer flow control with one atmosphere uniform glow discharge surface plasma," 36th AIAA Aerospace Science Meeting, AIAA Paper 1998-0328, Reno, NV, 1998.

[2]Roth, J.R., Sherman, D. M., and Wilkinson, S. P., "Electrohydrodynamic flow control with a glow-discharge surface plasma," *AIAA J.* Vol 38, 2000, pp. 1166–72.

[3]He, C., Corke, T., and Patel, M., "Plasma flaps and Slats: An Application of Weakly Ionized Plasma Actuators," *J. of Aircraft* , Vol. 46, No. 3, 2009, pp. 864-73.

[4]Benard, N., Braud P., Jolibois, J., Moreau, E.,"Airflow Reattachment Along a NACA 0015 Airfoil by Surfaces Dielectric Barrier Discharge Actuator – Time Resolved Particle Image Velocimetry Investigation," *4th Flow Control Conference*, AIAA 2008-4202 Seattle, WA, June 2008.

[5]Visbal, M.R., Gaitonde, D. V., Roy, S., "Control of Transitional and Turbulent Flows Using Plasma-Based Actuators," *AIAA Fluid Dynamics Conference and Exhibit*, AIAA Paper 2006-3230, San Francisco, CA, June, 2006.

[6]Post, M. and Corke, T., "Separation Control Using Plasma Actuators: Dynamic Stall Vortex Control on Oscillating Airfoil," *AIAA J.*, Vol. 44, No. 12, 2006, pp. 3125-35.

[7]Thomas, F. O., Kozlov, A., and Corke, T. C., "Plasma Actuators for Landing Gear Noise Reduction" *11th AIAA/CEAS Aeroacoustics Conference (26th AIAA Aeroacoustics Conference),* AIAA Paper 2005-3010, Monterey, CA, May, 2005.

[8]Huang, J., Corke, T. C., and Thomas, F. O., "Plasma Actuators for Separation Control of Low-Pressure Turbine Blades," *AIAA Journal*, Vol. 44, No. 1, 2006, pp 51- 57.

[9]Rizzetta, D. P. and Visbal, M.R, "Plasma-Based Flow-Control Strategies for Transitional Highly Loaded Low-Pressure Turbines," *J. Fluids Eng.*, Vol. 130, Issue 4, 2008.

[10]Sung, Y., Kim, W., Mungal, M. G., and Cappeli, M., "Aerodynamic Modification of Flow over Bluff Objects by Plasma Actuation," Experiments in Fluids, Vol. 41, No. 3, Sept. 2006, pp. 479–486.

[11]Moreau, E., "Airflow control by non-thermal plasma actuators," *J. Phys. D: Applied Physics*, Vol. 40, 2007, pp.605-636.

[12]Abe, T., Takizawa, Y., Sato,S., and Kimura, N.,. "A Parametric Experimental Study for Momentum Transfer by Plasma Actuator." *45th AIAA Aerospace Sciences Meeting and Exhibit*, AIAA Paper 2007-187,Reno, NV, January, 2007.

[13]Roth, J. R. and Dai, X., "Optimization of the Aerodynamic Plasma Actuator as an Electrohydrodynamic (EHD) Electrical Device," *44th AIAA Aerospace Sciences Meeting and Exhibit,* AIAA Paper 2006-1203, Reno, NV, January, 2006.

[14]Enloe, C. L., McLaughlin, T. E., VanDyken, R. D., Kachner, K. D., Jumper, E. J., and Corke T. C., "Mechanisms and Responses of a Single Dielectric Barrier Plasma Actuator: Plasma Morphology," *AIAA Journal*, Vol. 42, No. 3, 2004, pp 589-594.

[15]Enloe, C. L., McLaughlin, T. E., VanDyken, R. D., Kachner, K. D., Jumper, E. J., Corke, T. C., Post, M., and Haddad, O., "Mechanisms and Responses of a Single Dielectric Barrier Plasma Actuator: Geometric Effects," *AIAA Journal*, Vol. 42, No. 3, 2004, pp 595- 604.

[16]Forte, M., Jolibois, J., Pons, J., Moreau, E., Touchard, G., Cazalens, M., "Optimization of a dielectric barrier discharge actuator by stationary and non-stationary measurements of the induced flow velocity: application to flow control," *Exp Fluids*, Vol. 43, 2007, pp 917-928

[17]Hoskinson, A. R., Hershkowitz, N., and Ashpis, D. E., "Force measurements of single and double barrier DBD plasma actuators in quiescent air," *J. Phys. D: Applied Physics*, Vol. 41, 2008.

[18]Opaits, D. F., Zaidi, S. H., Shneider, M. N., Miles, R. B., Likhanskii, A. V., Macheret, S. O., and Ashpis, D., "Improving Thrust by Suppressing Charge Build-up in Pulsed DBD Plasma Actuators," *47th AIAA Aerospace Sciences Meeting Including The New Horizons Forum and Aerospace Exposition*, AIAA Paper 2009-487, Orlando, FL, January, 2009.

[19]Thomas, F. O., Corke, T. C., Iqbal, M., Kozlov, A., and Schatzman, D., "Optimization of Dielectric Barrier Discharge Plasma Actuators for Active Aerodynamic Flow Control," *AIAA Journal*, Vol. 47, No. 9, 2009, pp 2169- 2177.

[20]Kotsonis, M., Ghaemiy, S., Giepmanz, R., and Veldhuisx, L., "Experimental Study on the Body Force Field of Dielectric Barrier Discharge Actuators," *41st Plasmadynamics and Lasers Conference*, AIAA 2010-4630, 2010

[21]Model 9302 Atomizer, Instruction Manual, TSI, September, 2000

[22]DaVis 7.2, Instruction Manual, LaVision GmbH, December, 2007
[23]Baughn, J. W., Porter, C. O., Peterson, B. L., McLaughlin, T. E., Enloe, C. L., Font, G. I. and Baird, C., "Momentum transfer for an aerodynamic plasma actuator with an imposed boundary layer," *44th AIAA Aerospace Sciences Meeting*, AIAA Paper 2006-168, Reno, NV, January 2006
[24]Enloe, C. L., McLaughlin, T. E., and Font, G. I., "Parameterization of temporal structure in the single-dielectric-barrier aerodynamic plasma actuator," *AIAA Journal*, Vol. 44, No. 6, 2006, pp 1127-1136.
[25]Joussot, R., Hong, D., Rabat, H., Boucinha, V., Weber-Rozenbaum, R., and Leroy-Chesneau, A., "Thermal Characterization of a DBD Plasma Actuator: Dielectric Temperature Measurements using Infrared Thermography," *40th Fluid Dynamics Conference and Exhibit*, AIAA 2010-5102, Chicago, IL, 2010
[26]Jukes, T.N., Choi, K.-S., Segawa, T., and Yoshida, H., "Jet flow induced by a surface plasma actuator", *Proc. IMech. E.*, Part I: JSCE, Vol. 225, No 5, 2008, pp 347-356
[27]Hrubesh, L.W., Keene, L.E., and Latorre, V. R., "Dielectric properties of aerogels", *Journal of Materials Research*, Vol. 8, 1993, pp 1763-41